Paddy and Water Environment
https://doi.org/10.1007/s10333-026-01086-3

ARTICLE

Three-dimensional seismic analysis based on FE modeling using 3-D survey incorporating spatial variability of stiffness

Ivan Moharya Kasim[1] · **Shin-ichi Nishimura**[1] · **Toshifumi Shibata**[1]

Received: 12 February 2026 / Revised: 11 June 2026 / Accepted: 16 July 2026
© The Author(s) 2026

Abstract
Japan is one of the most earthquake-prone countries in the world, where a significant portion of disaster-related losses can be attributed to structural collapses. Thus, the inspection of geo-structures related to these earthquakes is important. Although conventional inspections are conducted by two-dimensional analyses, the actual behaviors of the structures are affected three-dimensionally. This has led to an increase in the demand for three-dimensional analyses. A three-dimensional survey has recently been developed, using an unmanned aerial vehicle (UAV), which has made the rebuilding of the three-dimensional shape of structures easier. Despite the development of this technique, it has not been adopted for the design of geo-structures. In this study, for the purpose of incorporating the three-dimensional survey technique into the design of geo-structures, an earth-fill dam is surveyed three-dimensionally by a drone, and a three-dimensional finite element model (FEM model) of the dam is made based on the survey results and the newly developed modeling approach. The spatial distribution of the ground stiffness is estimated based on screw weight sounding (SWS) test results, and then applied to the 3-D FEM modeling. Gaussian process regression (GPR), which serves as a geostatistical interpolation framework to transform sparse field measurements into continuous three-dimensional material property distributions for the FEM model, is employed for the spatial interpolation of the ground stiffness. Finally, the FEM model is applied to a seismic response analysis, and the locations of high acceleration and high shear stress inside the earth-fill dam are identified.

Keywords 3-dimensional survey · 3D FEM model · LIQCA · Seismic response characteristics

Introduction

There are many earth-fill dams in Japan, some of which have become old and degraded. It is important, therefore, to inspect the seismic resistance of such dams. For this purpose, it is necessary to investigate the strength inside the dams, and based on the strength distribution, a seismic analysis must be performed for large-scale earthquakes. In this study, a modeling method for the spatial distribution of the strength is presented, and an earth-fill dam is modeled three dimensionally. In many cases of old earth-fill dams, the shape of the embankment is not straight, but significantly curved. It is strongly recommended, therefore, that a 3-D analysis be used to assess the stability of these dams against earthquakes. Here, a 3-D analysis of an earth-fill dam is illustrated.

In recent years, due to advancements in unmanned aerial vehicle (UAV) technology, the taking of three-dimensional measurements has become easier. UAVs, more commonly known as drones, can be effectively employed to understand the situation of earth-fill dams in their entirety. This technique provides a low-cost alternative to classical aerial photogrammetry of small areas and large-scale topographic mapping or detailed 3D surface information. For photogrammetric mapping applications, many researchers have used UAV platforms for geomatics applications, instead of traditional photogrammetric methods, to produce digital surface models (DSMs) or digital terrain models (DTMs).

In this study, a three-dimensional finite element model (FEM model) of an earth dam is created using aerial photographs taken by a drone and the three-dimensional modeling of the underground. Although the authors proposed the basic procedure for 3-D FEM modeling back in 2021

✉ Shin-ichi Nishimura
theg1786@okayama-u.ac.jp

[1] Graduate School of Environmental and Life Science, Okayama University, 3-1-1 Tsushima-Naka, Kita-Ku, Okayama 700-8530, Japan

Published online: 06 October 2026

(Kaneshige et al. 2021), the procedure for 3-D subsurface modeling has not been completed. Since then, a method for a subsurface modeling scheme, in which the conventional approach is employed, has been added by the authors (Ohashi et al. 2022). Furthermore, an efficient procedure for the subsurface modeling of the spatial distribution of the soil properties is newly added in the present study.

Screw weight sounding (SWS) tests (Japanese Industrial Standards: JIS A 1221, 2020), and their more advanced version, screw driving sounding (SDS) tests (Orense et al. 2019), are in-situ geotechnical investigation methods used to assess the subsurface soil conditions. SWS tests can be conducted in narrow spaces or at sites that are difficult to access with large equipment. Since the raw results of SWS tests are relatively simple measurements of the penetration resistance, their interpretation and application often involve empirical relationships, and the measured values need to be interpolated spatially. For the spatial interpolation task, Gaussian process regression (GPR) is employed here. GPR (Rasmussen and Williams 2006) is well-suited for modeling spatially correlated data and providing estimates with associated uncertainty.

In the present study, firstly, an embankment model is created using three-dimensional measurements taken by a drone. Secondly, the results of SWS tests are applied to create a three-dimensional model of the subsurface, and then interpolated in three dimensions by GPR. Finally, a three-dimensional seismic response analysis is performed on the three-dimensional model. A high-precision analysis is achieved by obtaining three-dimensional information on the ground surface and the subsurface ground.

Studies dealing with the three-dimensional analysis of dam embankments have been carried out. Xu et al. (2012) performed a three-dimensional finite element analysis to evaluate the deformation of concrete face rockfill dams. Mosadegh et al. (2021) indicated that a 3D analysis might be more appropriate than a 2D analysis for studying the seismic response of heterogeneous earthen dams, especially when extensive CPTu (piezocone penetration test) information is available to model the dams. Chen et al. (2020) performed a seismic analysis of hardfill dams, considering the spatial variability of the material parameters, and proposed a method for examining the relationship between a random field and the dam response.

It is well known that understanding the spatial distribution of the geotechnical properties has a noticeable influence on the analysis of a ground. Guan and Wang (2022) succeeded in obtaining a random field of safety factors for ground liquefaction by interpolating the limited CPT test results using Bayesian compressive sampling and a Monte Carlo simulation. Zhao et al. (2021) also studied the efficient selection of CPT sounding locations for determining the spatial distribution, as the spatial variability of the ground plays an important role in geo-structural analyses. In addition, Chen et al. (2015) addressed the spatial variability of the soil parameters interpolated by geostatistical methods to assess the liquefaction potential.

GPR, which has recently attracted attention in the field of pattern recognition as a general regression theory, has also been a subject of research in the field of civil engineering. Yoshida et al. (2021) proposed a method for simultaneously estimating the trend and random components of geotechnical properties at an arbitrary point using GPR, which superimposes multiple probability fields. Ching et al. (2022) compared trend models for spatial variability in the ground, between GPR and sparse Bayesian learning (SBL), and concluded that the GPR model outperformed the SBL model in both 2D and 3D real examples.

In recent years, data-driven approaches integrating machine learning algorithms with finite element simulations have increasingly attracted attention in geotechnical earthquake engineering. In addition to geostatistical methods such as GPR, neural-network-based approaches have also been explored for predicting seismic topographic effects and nonlinear response characteristics of geo-structures (e.g., Jiang et al. 2024). These developments indicate a growing trend toward hybrid frameworks that combine physics-based numerical simulations with data-driven spatial characterization techniques.

In contrast to these previous studies, the purpose of the present study is to demonstrate that the three-dimensional modelling of the ground surface and the underground, using three-dimensional measurements, sounding test results, and the unified finite element method, can work effectively for real problems. The procedure for coupling 3D ground surface modelling and 3D underground modelling, based on the SWS and through the use of GPR, is the relevant novelty point of this study.

SWS tests

In this study, an analysis was carried out for an earth-fill dam, Site K, in Okayama, Japan. The sounding intervals were adjusted so that the parameters necessary for the application of geostatistical modelings could be applied. The SWS test is a static test, which is very efficient and suitable for obtaining spatial information on soil structures. In addition, since it is a very compact test, it can be applied to sites located in narrow spaces, such as the site of concern in this study.

The test method is to firstly apply a load to the screw point in stages from 50 N to 1 kN via a rod, and then to determine the relationship between the load (W_{sw}) and the

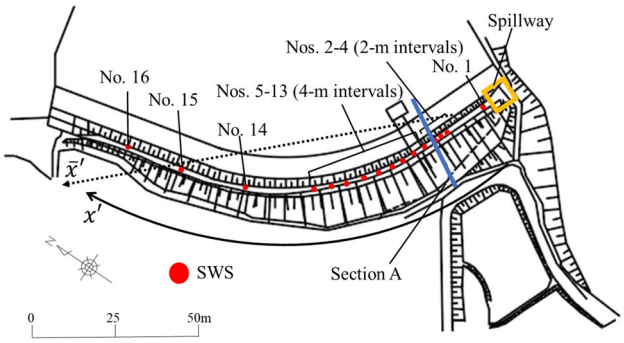

Fig. 1 Plan view of Site K and SWS test points on studied earth dam

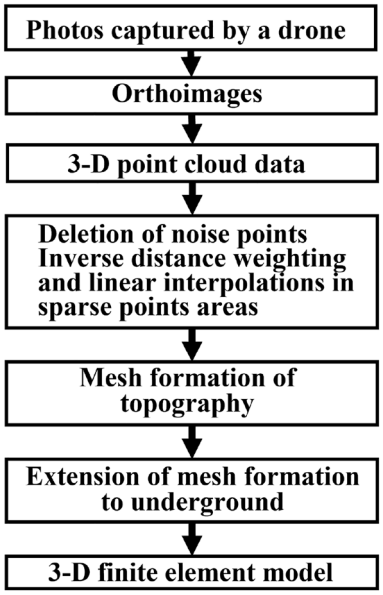

Fig. 2 Algorithm of 3-D survey and modeling

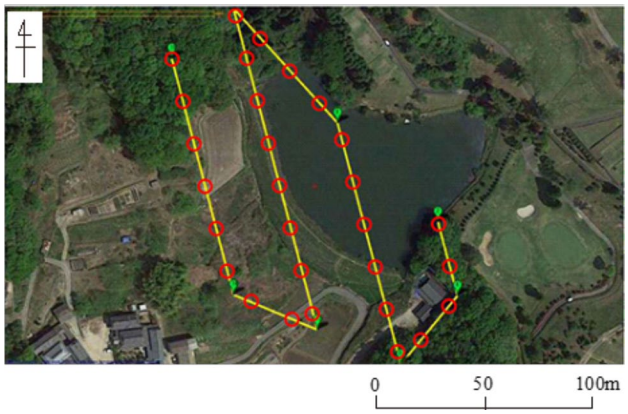

Fig. 3 Flight path of drone over studied site. (Yellow line: planned flight path Green dots: direction change points Red circles: actual filming positions)

amount of penetration. If the rod does not penetrate 25 cm, even when a load of 1 kN is applied, the rod is to be rotated to achieve penetration and the number of half rotations (N_a) is to be counted until it penetrates 25 cm. The measured number of half-rotations, N_a, is then converted to N_{sw}, which represents the normalized number of half-rotations required for 1 m of penetration. These measurements are to be taken every 25 cm of penetration.

Equation (1) is a regression equation between the N-value, obtained from the standard penetration test for sandy soil, and the results of the SWS tests, presented by Inada (1960), from which the converted N-value (N_{SWS}) is obtained for sandy soil.

$$N_{SWS} = 0.002W_{SW} + 0.067N_{SW} \quad (1)$$

where N_{SW} is the number of half rotations and W_{SW}(N) is the total weight of the loads. Figure 1 shows a plan view of Site K and the locations (16 points) where the SWS tests were conducted along the x'-axis parallel to the embankment axis.

Since the soil of the embankment in studied site consists of sandy material, Eq. (1) is applied appropriately. Although Eq. (1) is an old empirical equation, it is still frequently employed for the designs. Nishimura et al. (2009) verified the accuracy of the equation by the additional data.

Three-dimensional finite element model

A three-dimensional finite element model is created from aerial photographs taken by a drone. The outline of the 3-D modelling is presented in Fig. 2. Three-dimensional measurements are taken by a drone in order to model the shape of the dam in detail. The procedures for photographing the dam and creating a three-dimensional finite element model are shown below.

The drone is an Enroot QC730, and the camera is a Sony α6000 with an effective pixel count of approximately 24.3 megapixels. Firstly, the drone is flown back and forth over the site at an altitude of 60 m and a speed of 5 m/s. The camera is fixed to face directly downwards and is used to take images of the dam. The actual flight path is shown in Fig. 3. The yellow line in the diagram shows the planned flight path, the green dots indicate the direction change points, and the red circles indicate the actual filming positions. The overlap rate is set to 83.0%, while the side-wrap rate is set to 60.0%. A visual representation of the degree of overlap is shown in Fig. 4. In this figure, the white rectangles represent the photographed areas and the dark red areas are the actual paths being measured. The red dots represent the traverse survey points required for orientation. The green dots indicate the direction change points, as seen in Fig. 3. For these measurements, the horizontal error is 4 cm and the elevation

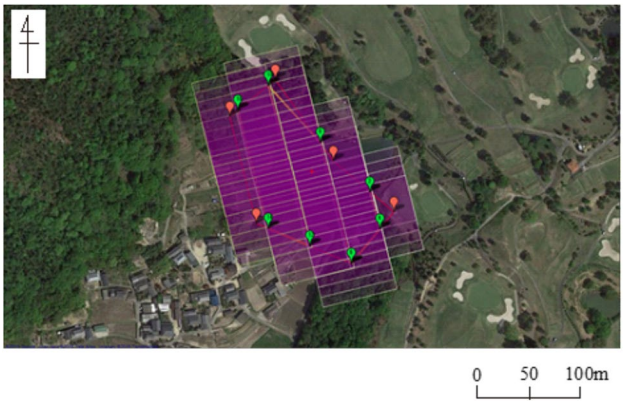

Fig. 4 Depiction of degree of overlapping of photography. (White rectangles: photographed areas)

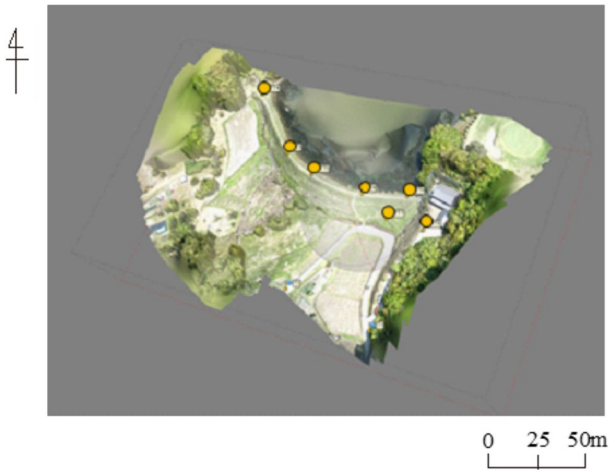

Fig. 5 Reconstructed figure of earth-fill dam site based on 3-D data. (Orange points: Orientations)

error is 5 cm at a flight height of 60 m (compared to the terrestrial laser scanner).

Orthoimages and point cloud data are created using Agisoft PhotoScan Professional ver. 1.2.6 (Agisoft). Firstly, the image data are imported into the software. Next, stereo matching is performed to create coarse point cloud data by analyzing the principal points of each photograph. Next, mesh data are created from the point cloud data and the topography is reproduced (Fig. 5). After that, the coordinates are input to the orientations in the image, which are presented by red points. The input values of Photoscan are the plane coordinates and the elevations of the traverse survey points, route survey transect points, and GNSS (Global Navigation Satellite System) survey points on road surfaces and embankment slopes. Finally, high-density point cloud data are generated by stereo matching the photographs. The point cloud data created by Photoscan contain unnecessary points, such as those representing surrounding vegetation and shadows on the pond, which need to be deleted. Therefore, the point cloud data are imported into ScanSurveyZ Ver.1.2.0 (Be System) and the unnecessary point clouds are deleted. In the point cloud deletion, triangulation, color (illumination), grid, density, and ground surface are considered.

Filtering by triangulation is a method for extracting and deleting points that are more than a specified distance away from the formed triangulation or too high or low from the surface. Filtering by color (illumination) is a method for extracting and deleting points with specified RGB (red, green, and blue) values and light intensity. Filtering by a grid is a method for extracting and deleting points other than the specified elevation value and remaining points in the grid. Filtering by density is a method for extracting and deleting unnecessary points (noise) that appear in the air based on their density. In this study, the shape of the ground surface is the most important information for the analysis of the embankment. Therefore, filtering by the elevation of the ground surface, which is a method for extracting the points with the lowest values, is selected. The deletion of the point cloud is carried out, while the shapes of the cross sections along the longitudinal and transverse directions of the embankment are checked. When point cloud data are created using Photoscan, the water surface is judged as noise and automatically removed. Therefore, PETs (point cloud edit tools) Ver.1 (Iwasaki) are used to add point clouds to the pond area to create the shape of the pond bottom at intervals of approximately 3 m in the horizontal direction.

Since 3D mesh data may not be generated in areas of coarse point clouds, interpolation is performed in this study using PETs. Firstly, the point cloud data output from ScanSurveyZ are imported into the PETs. Next, IDW (inverse distance weighting) interpolation and linear interpolation are performed to create additional points, and finally, the corrected point cloud data are output (Fig. 6). Approximately 40 photographs are taken to generate the point cloud, and 11 points are used for the orientation points.

For the creation of the 3D model, finite element modeling functions are newly developed in this study. These functions are added to ScanSurveyZ for the finite element modeling in order to construct a 3D model, and finite elements are created from the 3D point cloud data.

Nodal intervals for the longitudinal and the transversal directions are set at 0.5-m intervals from the central axis of the embankment to 10 m, at 1-m intervals from 10 to 12 m, at 2-m intervals from 12 to 18 m, and at 3-m intervals thereafter on either side. In the height direction, based on the highest elevation, the intervals are set at 0.5-m intervals from 0 to − 13.5 m, at 1-m intervals from − 13.5 to − 14.5 m, at 5-m intervals from − 14.5 to − 24.5 m, and at 10-m intervals below that.

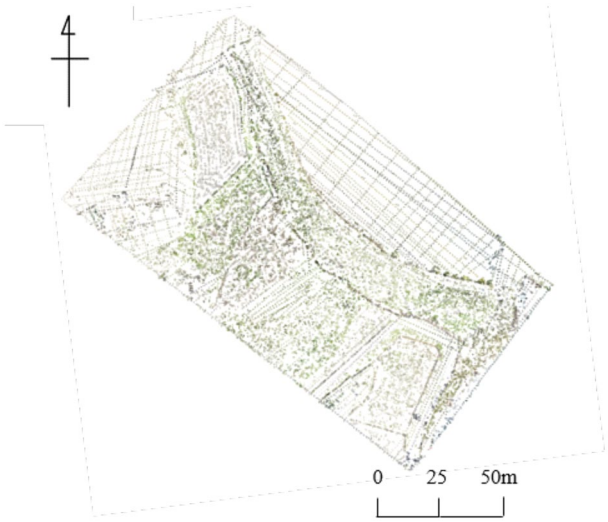

Fig. 6 Point group data for 3-D model

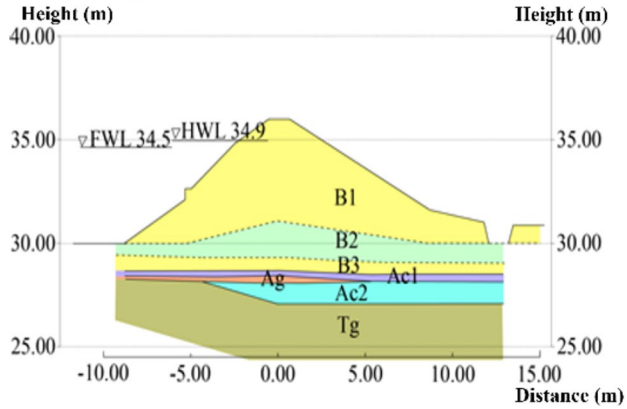

Fig. 7 Cross section of geological stratums

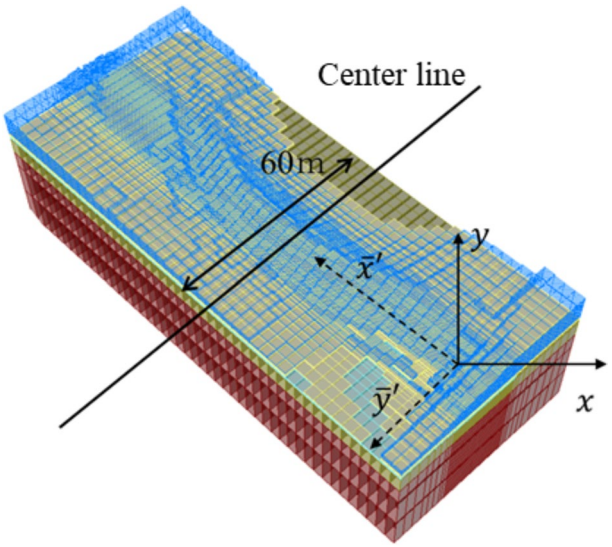

Fig. 8. 3-D model of embankment area

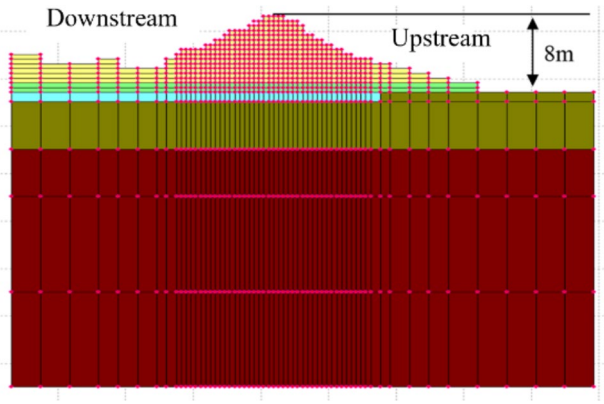

Fig. 9 Cross section of center line of 3-D model

The nodal coordinates of the finite elements are set to the *x*-axis for the east–west direction and to the *y*-axis for the north–south direction. After the mesh has been created, the unnecessary elements at the water surface of the earth dam are deleted, and the bottom of the earth dam is reproduced. Since the geological survey was conducted in the target area, the estimated cross-sectional map, prepared based on the results of standard penetration tests (SPTs) with borings and described in the geological survey report, is used for this work. The borings were carried out on Section A, presented in Fig. 1, and the identified geological cross section of Section A is presented in Fig. 7. The geology is classified into five layers, namely, [B1], [B2, B3], [Ac1, Ag, Ac2], [Tg], and [Foundation rock], as seen in Fig. 7. However, the Ac1, Ac2, and Ag layers are treated the same as the Ac layer because they are thin. Figure 8 provides an overall view of the model, while Fig. 9 provides the cross section of the central part of the model. The color coding in these two figures indicates the material classification, which is shown in Fig. 7. Nodes and elements were added to the sides of the model, and the analysis domain was extended to a square 50 times the width of the embankment to reduce the influence of the boundaries. The *x*-axis and *y*-axis in the figure were set in the east–west and north–south directions, respectively, and the *z*-axis was set in the vertical direction. The whole analytical model, including the boundaries, is depicted in Fig. 10.

Interpolation based on geostatistical models

Determination of statistical model of SWS N-values using GPR

The spatial distribution of the ground strength parameters is commonly represented through statistical modeling techniques. Given the inherently discrete nature of the data acquired from geotechnical sounding tests, interpolation

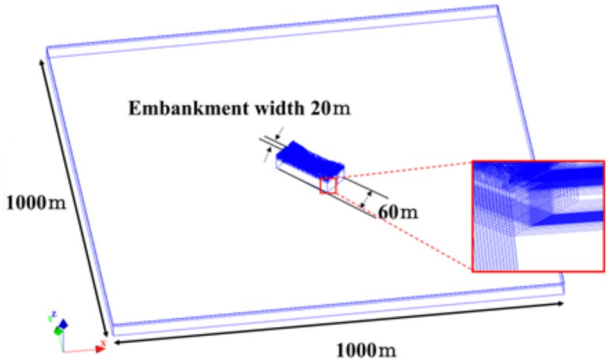

Fig. 10 Entire analytical area including boundaries

between sampling points becomes essential for constructing a continuous representation of the subsurface properties. In the present investigation, Gaussian process regression (GPR) methodology, as described by Rasmussen and Williams (2006), is employed to estimate both the trend and random components of the ground properties, thereby establishing a comprehensive statistical model. The GPR-based estimation procedure, as adapted from Yoshida et al. (2021), is performed as follows.

When considering an observation vector s, sampled from a random field, a linear function Hr is defined to extract the observed portion from a zero-mean Gaussian random field vector, r, which is partitioned as

$$r^T = \{r_1^T, r_2^T\} \tag{2}$$

where r_1 represents variables at the observation locations and r_2 denotes variables in regions requiring estimation. The observation equation can be reformulated as

$$s = Hr = [I0]\left\{ \begin{array}{c} r_1 \\ r_2 \end{array} \right\} + \nu \tag{3}$$

where I denotes the identity matrix, 0 denotes a zero matrix, and v is the observation noise. Prior covariance matrix M, corresponding to r_1 and r_2, is directly calculated by one of the covariance functions and defined as

$$M = \left[\begin{array}{cc} M_{11} & M_{12} \\ M_{12}^T & M_{22} \end{array} \right] \tag{4}$$

The expected value for r is subsequently given by Eq. (5).

$$\left\{ \begin{array}{c} \hat{r}_1 \\ \hat{r}_2 \end{array} \right\} = \left[\begin{array}{c} M_{11} \\ M_{12}^T \end{array} \right] [M_{11} + R]^{-1} s \tag{5}$$

where R is the covariance matrix of v.

This formulation can be generalized to accommodate the superposition of n random fields.

$$r^T = (r_1^T, r_2^T) = \left(\sum_{k=1}^{n} w_{k,1}^T, \sum_{k=1}^{n} w_{k,2}^T \right) \tag{6}$$

Consider the case where observation vector s is sampled from the combined effect of multiple random fields $w_{k,1}$, $w_{k,2}$, $k=1, 2, \ldots$, and n. These random fields include observation noise v. It should be noted that observation noise v need not be independent, i.e., covariance matrix R does not need to be diagonal. The covariance matrices of random fields $w_{k,1}$ and $w_{k,2}$ are $M_{k,1}$ and $M_{k,2}$, respectively. Random fields $w_{k,1}$ and $w_{k,2}$ depend on observation data s, and can be estimated by considering the superposition of the remaining random fields as noise v in Eq. (5).

$$\left\{ \begin{array}{c} w_{k,1} \\ w_{k,2} \end{array} \right\} = \left[\begin{array}{c} M_{k,11} \\ M_{k,12}^T \end{array} \right] \left[\sum_{l=1}^{n} M_{l,11} \right]^{-1} s \tag{7}$$

The specific case of $n=2$, namely, $s=w_{1,1}+w_{2,1}$ in Eq. (6), is examined in this study. Random fields $w_{1,1}$ and $w_{2,1}$ are designated as the trend and random components, respectively.

From a machine learning perspective, the present formulation is conceptually equivalent to the composite kernel framework widely used in Gaussian process modeling, where multiple covariance kernels are superimposed to represent different spatial characteristics simultaneously. In the present study, the additive covariance structure enables the decomposition of the spatial variability into long-wavelength trend components and short-wavelength local fluctuations within a unified Bayesian framework. This formulation bypasses the conventional two-step detrending procedure frequently adopted in geostatistical analyses.

Similar concepts have recently been explored in the machine learning community for automated kernel composition and probabilistic spatial prediction (Duvenaud et al. 2013; Zhao et al. 2026). The present study demonstrates the applicability of such composite covariance concepts to the spatial characterization of embankment materials in geotechnical earthquake engineering.

In this approach, the traditional method, based on the selection of the basis function, is substituted with the selection of the covariance function and parameter estimation. The maximum likelihood estimation (MLE) technique is employed to determine parameters such as the scale of fluctuation (SOF) δ and standard deviation σ within the covariance function associated with matrix M. The log-likelihood function, ln L, is expressed as

$$lnL = -\frac{1}{2} s^T \left(\sum_{l=1}^{n} M_{l,11} \right)^{-1} s - \frac{1}{2} \ln \left| \sum_{l=1}^{n} M_{l,11} \right| + \frac{m}{2} \ln (2\pi) \tag{8}$$

where m represents the number of data points. Optimization techniques are applied to determine the covariance function parameters that maximize the log-likelihood.

For the purpose of estimating the spatial distribution of the ground strength, the x'-axis, oriented along the embankment with its origin at test site No. 1 (0 m), is treated as a linear axis for analytical simplicity. In the vertical direction, the z'-axis is established in the depth dimension with the origin at the ground surface. The kernel function employed in this study is defined by Eq. (9), as follows:

$$k = \sigma^2 exp\left(-\pi\left(\frac{\left|x_i' - x_j'\right|}{\delta_x}\right)^2 - \pi\left(\frac{\left|z_i' - z_j'\right|}{\delta_z}\right)^2\right) \tag{9}$$

where δ is the scale of fluctuation (SOF) and σ is the standard deviation of the random field.

Since the seismic analysis is conducted three-dimensionally, the statistical model must be extended to a three-dimensional representation. The distance between two points, dh, is defined under the assumption of statistical homogeneity across the xy-plane.

The three-dimensional kernel function is formulated as

$$k = \sigma^2 exp\left(-\pi\left(\frac{dh}{\delta_h}\right)^2 - \pi\left(\frac{dv}{\delta_v}\right)^2\right) \tag{10}$$

where $dh = \sqrt{\left(\overline{x}_i' - \overline{x}_j'\right)^2 + \left(\overline{y}_i' - \overline{y}_j'\right)^2}$, $dv = \left|z_i' - z_j'\right|$, $\delta_v = \delta_z$, and horizontally statistical homogeneity, $\delta_h = \delta_x$, is assumed.

For the three-dimensional covariance expressed in Eq. (10), the total number of parameters is six (comprising horizontal SOFs, vertical SOFs, and standard deviations for both trend and random components). Table 1 presents the parameters obtained through the maximum likelihood method. Figure 11 illustrates the depth profiles of the trend estimated by GPR alongside the measured values, where the red lines denote the trend and the blue points represent the observed data.

The scale of fluctuation (SOF) serves as a metric for the distance within which properties exhibit significant correlation (Vanmarcke 2010). A larger SOF indicates a slower rate of property fluctuation with increasing distance.

Estimation of ground stiffness distribution

In this study, the estimated N-values (N_{SWS}) are incorporated into the finite element model. Although basically, the soil properties of the ground are determined based on the geological survey report of the study site, the stiffness is estimated derived from the N-values herein. To interpolate the stiffness values derived from the N-values, GPR—functionally analogous to kriging—is applied. The interpolation process follows the random fields derived from Eq. (7).

Subsequently, the coordinates of the ground distribution interpolated by GPR undergo transformation into the FEM model's coordinate system (x- and y-axes) through rotation by angle θ between the x'-axis and the x-axis. This transformation is necessary because the FEM model coordinates align with the digital elevation model (DEM) data captured by the drone, which differ from the those of the GPR coordinate system. When the planar coordinates of the x'-axis are (x', y'), the transformation to (x, y) coordinates is expressed by Eqs. (11) and (12), where θ = 135° (see Fig. 8).

$$x = \overline{x}' \cos\theta - \overline{y}' \sin\theta \tag{11}$$

$$y = \overline{x}' \sin\theta + \overline{y}' \cos\theta \tag{12}$$

In this study, two distinct models are developed for a comparative analysis to assess the influence of soil heterogeneity: one model is homogeneously divided along the embankment axis without incorporating the sounding test data, while the other model is heterogeneously divided based on the sounding data. The homogeneous model follows the geological cross-sectional map (Fig. 7) for material classification along the dam axis. Figures 12 and 13 display the N-value distributions for the homogeneous model along the dam axis and the inhomogeneous model at Site K, respectively. In the inhomogeneous model, material classification is performed according to the N-value distribution.

Analytical model

Material constants

All analyses in this study employ linear elastic formulations. The three-dimensional seismic response analysis is conducted using LIQCA3D (Development Group of

Table 1 Estimated parameters

Trend component			Random component		
Horizontal scale of fluctuation, $\delta_{t,h}$ (m)	Vertical scale of fluctuation, $\delta_{t,v}$ (m)	Standard deviation, σ_t	Horizontal scale of fluctuation, $\delta_{r,h}$ (m)	Vertical scale of fluctuation, $\delta_{r,v}$ (m)	Standard deviation, σ_r
17.52	6.634	1.172	14.08	0.728	0.504

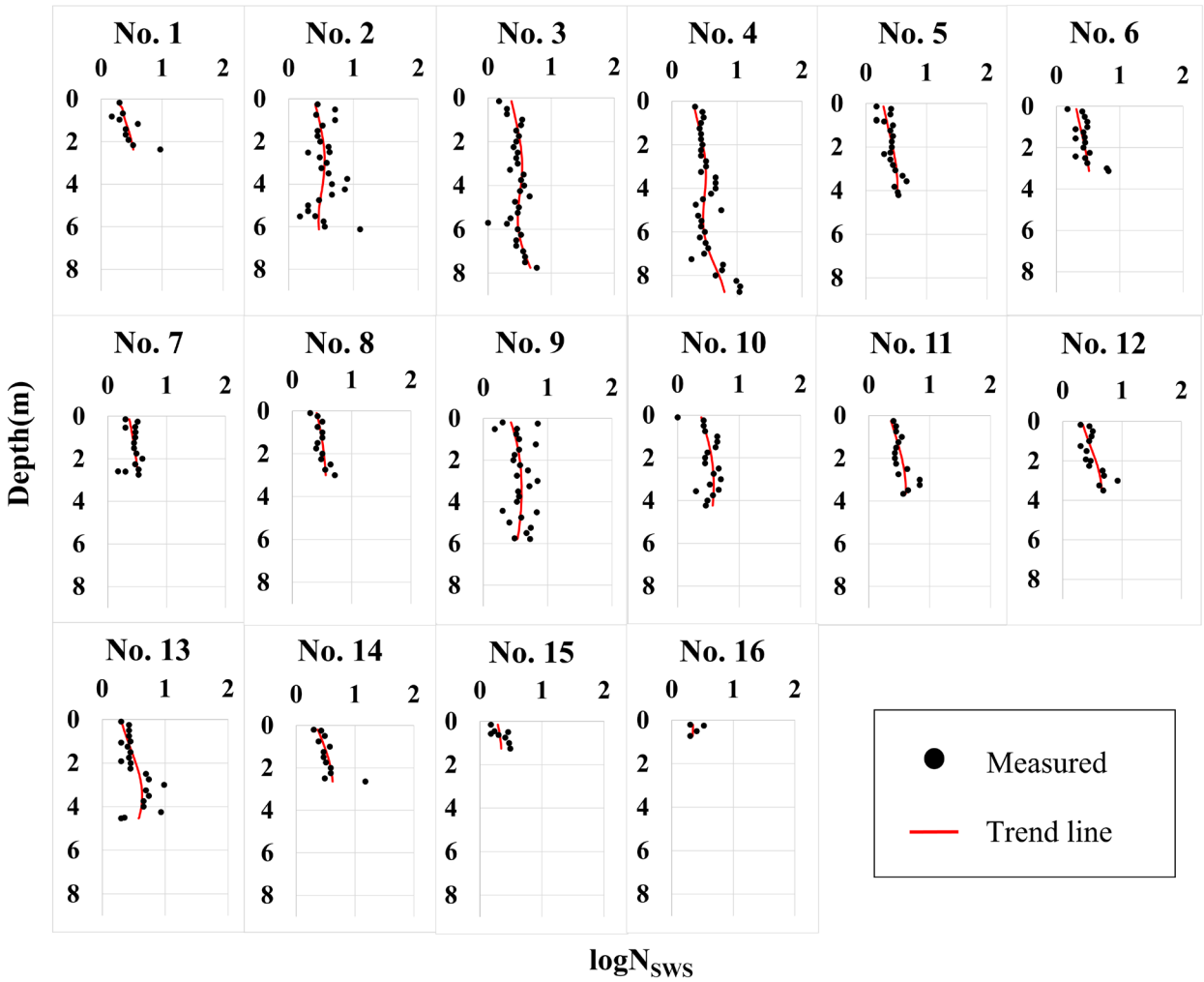

Fig. 11 Measured values and trend function of log N_{sws}

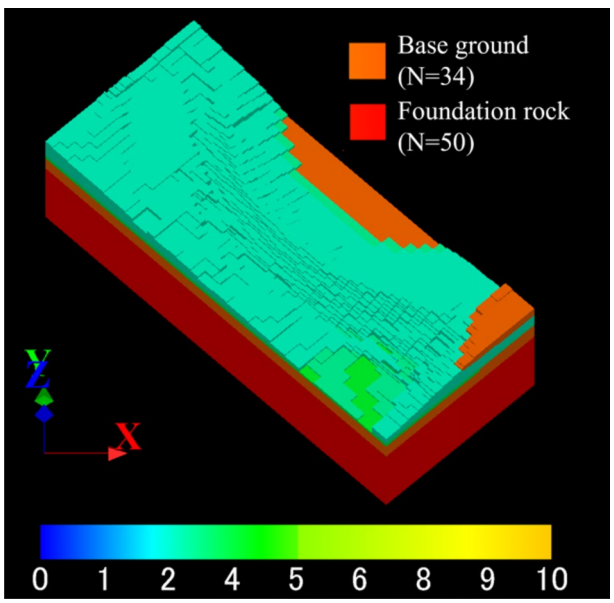

Fig. 12 Spatial distribution of N-values (Homogeneous model)

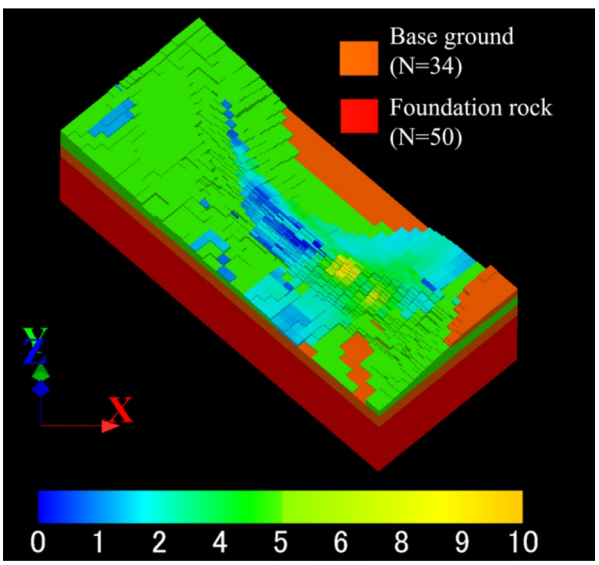

Fig. 13 Spatial distribution of N-values (Inhomogeneous model)

Liquefaction Analysis Code LIQCA 2021). In this study, the primary objective is to establish and validate a practical workflow for integrating UAV-based three-dimensional surface reconstruction, SWS-based subsurface characterization, and geostatistical interpolation into a unified 3D FEM framework. Therefore, a linear elastic constitutive formulation is adopted as an initial approximation to evaluate the influence of three-dimensional geometry and spatial heterogeneity on the seismic response characteristics. It is recognized that earth-fill dams subjected to strong earthquake motions exhibit significant nonlinear behavior, including shear modulus degradation, strain-dependent damping, and plastic deformation. Consequently, the present analysis should be interpreted as a preliminary evaluation of the spatial response tendency rather than a complete prediction of nonlinear seismic performance. The incorporation of advanced constitutive models within LIQCA3D will be addressed in future studies.

For the elastic constant determination, Young's modulus E is calculated using Eq. (13) (Japan Road Association, 2012), which provides a conversion formula based on the standard penetration test (SPT) N-value. This equation, commonly applied in the design of embankments and sand layers, assumes conditions where the strain reaches relatively large magnitudes.

$$E = 2800N \tag{13}$$

$$\mu = \frac{E}{2(1+\nu)} \tag{14}$$

$$\lambda = \frac{\nu}{(1-2\nu)(1+\nu)}E \tag{15}$$

where λ is Lame's first constant (kN/m^2), μ is Lame's second constant (kN/m^2), E is Young's modulus (kN/m ^{2}), N is the N-value, and ν is Poisson's ratio.

Poisson's ratio ν is assigned a value of 0.3, consistent with standard geotechnical practice. The calculated geotechnical constants for each material are presented in Table 2. Permeability k is also included for saturated materials, as permeability tests were conducted for these specific layers.

Young's modulus of Eq. (13) is not used as a modulus corresponding to the initial small strain, but is corresponding to the modulus of the rather large strain, since the strong seismic motion is analyzed.

The stiffness of the embankment layers, B1, B2, and B3 are interpolated as a single layer by the GPR. The three layers are treated as a single layer for the GPR, since the stiffness of the layers does not depict clear distinctions, and looks sequential.

Boundary conditions

The viscous boundary condition at the model base was introduced to reduce artificial reflection of outgoing seismic waves at the truncated numerical boundary. In addition, the analytical domain was extended sufficiently beyond the embankment region to further minimize boundary-induced amplification effects during the dynamic response analysis.

The boundary conditions are defined as follows: the bottom boundary is employed as a viscous boundary, lateral boundaries along the x-axis direction are constrained against y-displacement, lateral boundaries along the y-axis direction are constrained against x-displacement, and the four corner nodes are fixed against x–y displacement while permitting vertical roller support for the z-axis direction.

Table 2 Ground properties

Layer	N-value	Young's modulus E (kN/m^2)	Lame's first constant λ (kN/m^2)	Lame's second constant μ (kN/m^2)	Effective overburden pressure σ'$_v$ (kN/m^2)	Hydraulic conductivity k (m/s)
(a) Homogeneous model along direction of dam axis						
B1	3	8.4×10^3	4.85×10^3	3.23×10^3	18.5	–
B2, B3	3.7	1.04×10^4	6.00×10^3	3.99×10^3	46.3	4.83×10^{-7}
Ac	5.4	1.51×10^4	8.72×10^3	5.82×10^3	83.3	3.61×10^{-9}
Tg	34	9.52×10^4	5.49×10^4	3.66×10^4	139	3.45×10^{-8}
Base ground	34	9.52×10^4	5.49×10^4	3.66×10^4	28	3.45×10^{-8}
Foundation rock	50	1.40×10^5	8.08×10^4	5.38×10^4	421	–
(b) Inhomogeneous model						
B1	By SWS	From Eq. (14)	From Eq. (16)	From Eq. (15)	18.5	–
B2, B3					46.3	4.83×10^{-7}
Ac	5.4	1.51×10^4	8.72×10^3	5.82×10^3	83.3	3.61×10^{-9}
Tg	34	9.52×10^4	5.49×10^4	3.66×10^4	139	3.45×10^{-8}
Base ground	34	9.52×10^4	5.49×10^4	3.66×10^4	28	3.45×10^{-8}
Foundation rock	50	1.40×10^5	8.08×10^4	5.38×10^4	421	–

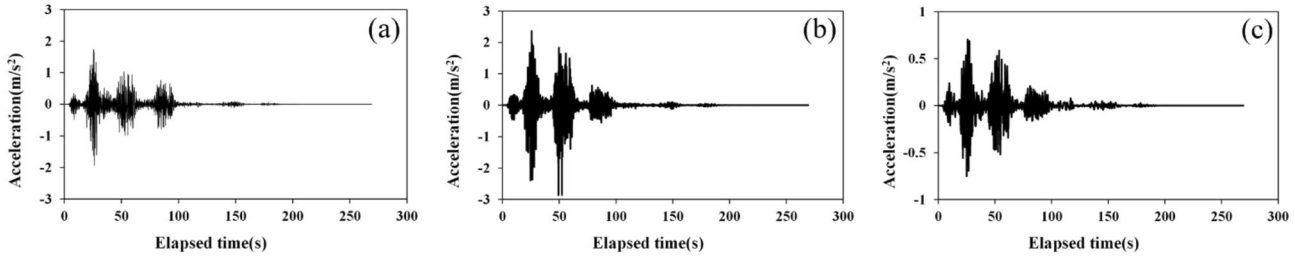

Fig. 14 Input seismic waveforms in **a** transversal direction to dam axis, **b** direction of dam axis, and **c** vertical direction

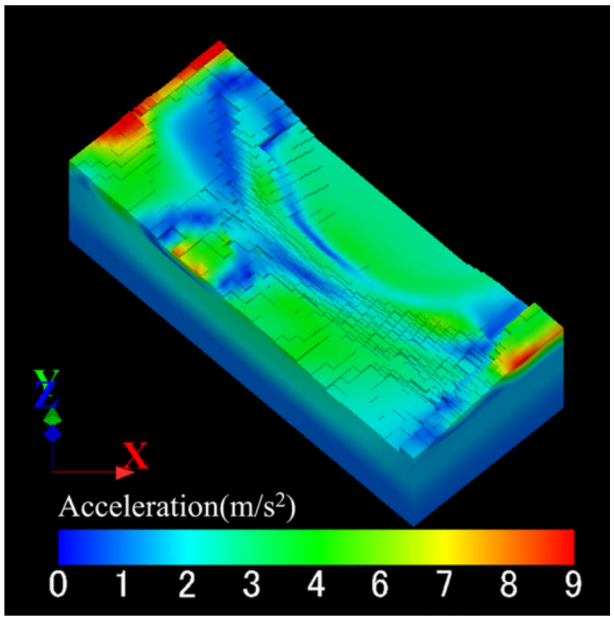

Fig. 15 Distribution of accelerations (Homogeneous model)

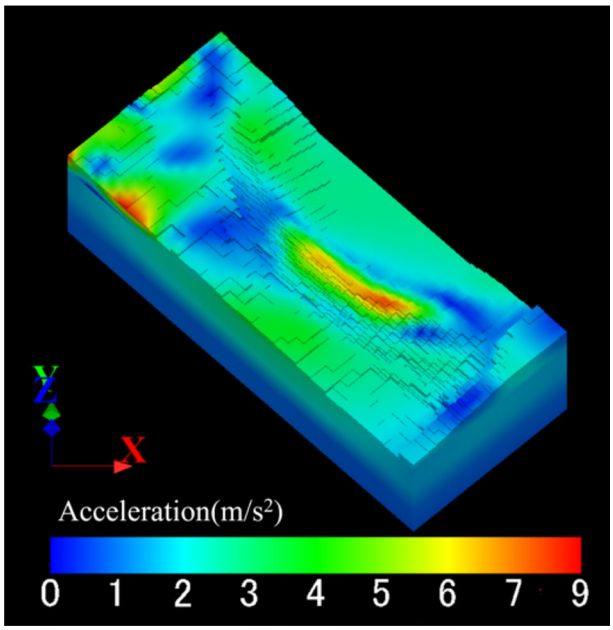

Fig. 16 Distribution of accelerations (Inhomogeneous model)

Both the bottom and all side boundaries are designated as undrained boundaries.

Input earthquake motion

The input ground motions are selected from the Nankai Trough earthquake scenario database published by the Cabinet Office of Japan. The adopted waveforms correspond to a large subduction-type earthquake scenario with a moment magnitude of approximately Mw 8–9. The sample wave corresponds to the engineering bedrock of the studied site in south-west region of Okayama, Japan, is employed. In the present study, the original sample time series of acceleration is applied for the seismic analysis without spectral matching.

For comparison with response acceleration, the acceleration components in the x-axis and y-axis directions are divided into those of the longitudinal and orthogonal directions along the embankment's axial direction. The acceleration waveforms of the input seismic motion are illustrated in Fig. 14.

Results of seismic response analysis

The analysis results for both the homogeneous model along the dam axis direction and the inhomogeneous model are presented in Figs. 15–29. Figures 15 and 16 display contour plots of the maximum accelerations at the peak of the input earthquake motion, specifically 25 s after the initiation of seismic activity, corresponding to the maximum input acceleration. Figures 17 and 18 depict the response accelerations at the surface nodes of the central section. Figures 19 and 20 illustrate the response velocities at the same location, while Figs. 21 and 22 present the response displacements.

In addition, to evaluate the shear stress, the $\sqrt{2J_2}$ distribution diagram obtained from the second invariant of the deviatoric stress (J_2) is given. The second invariant of the deviatoric stress is calculated by Eq. (16).

$$J_2 = \frac{1}{6}\left\{(\sigma_x - \sigma_y)^2 + (\sigma_y - \sigma_z)^2 + (\sigma_z - \sigma_x)^2\right\} + \tau_{xy}^2 + \tau_{yz}^2 + \tau_{zx}^2 \quad (16)$$

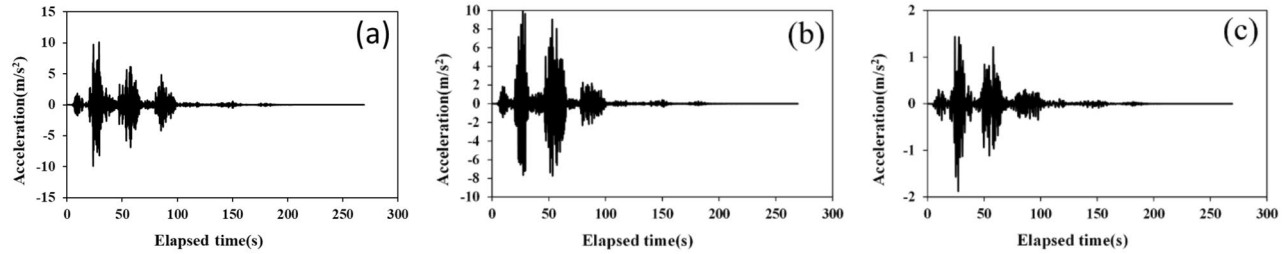

Fig. 17 Response accelerations of **a** transversal direction to dam axis, **b** direction of dam axis, and **c** vertical direction (Homogeneous model)

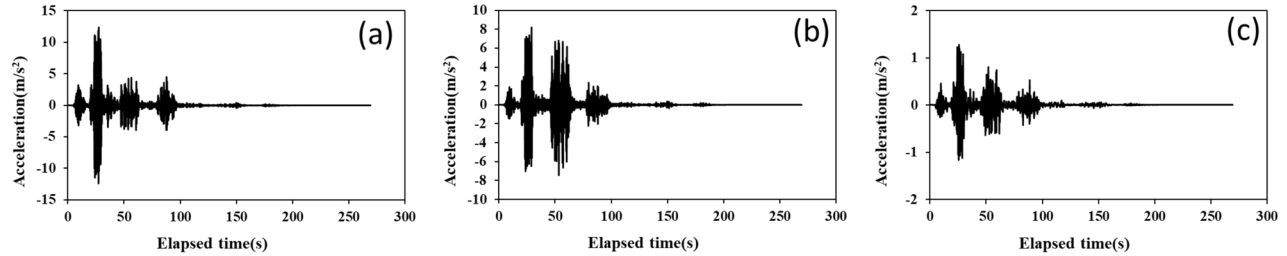

Fig. 18 Response accelerations of **a** transversal direction to dam axis, **b** direction of dam axis, and **c** vertical direction (Inhomogeneous model)

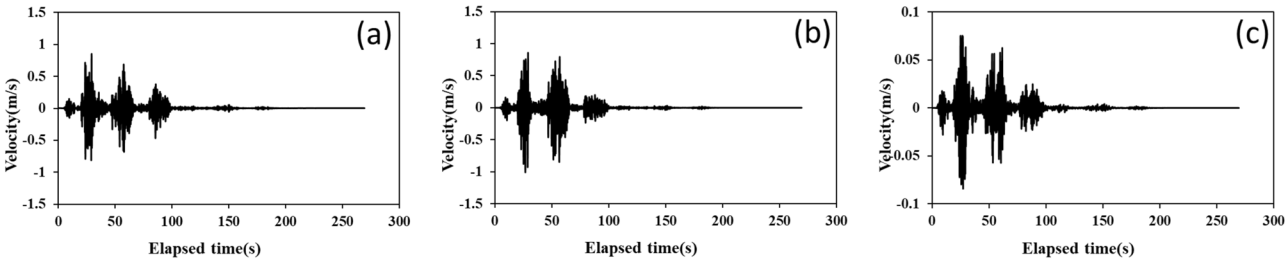

Fig. 19 Response velocities of **a** transversal direction to dam axis, **b** direction of dam axis, and **c** vertical direction (Homogeneous model)

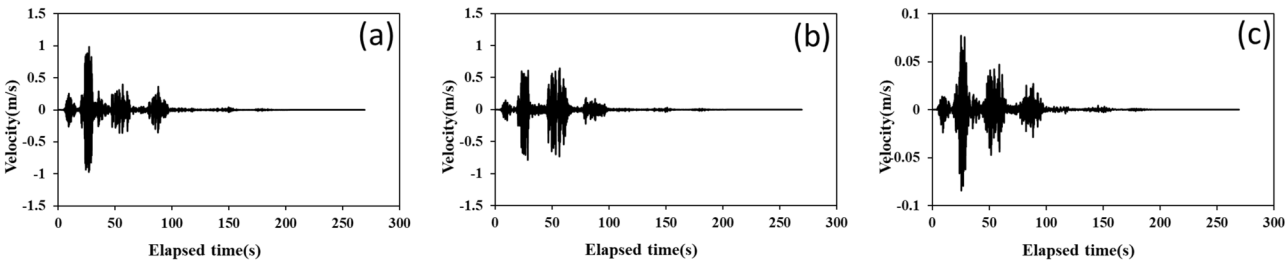

Fig. 20 Response velocities of **a** transversal direction to dam axis, **b** direction of dam axis, and **c** vertical direction (Inhomogeneous model)

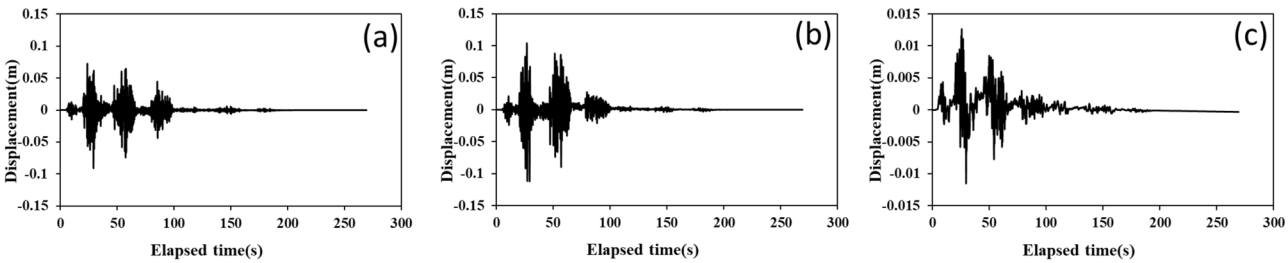

Fig. 21 Response displacements of **a** transversal direction to dam axis, **b** direction of dam axis, and **c** vertical direction (Homogeneous model)

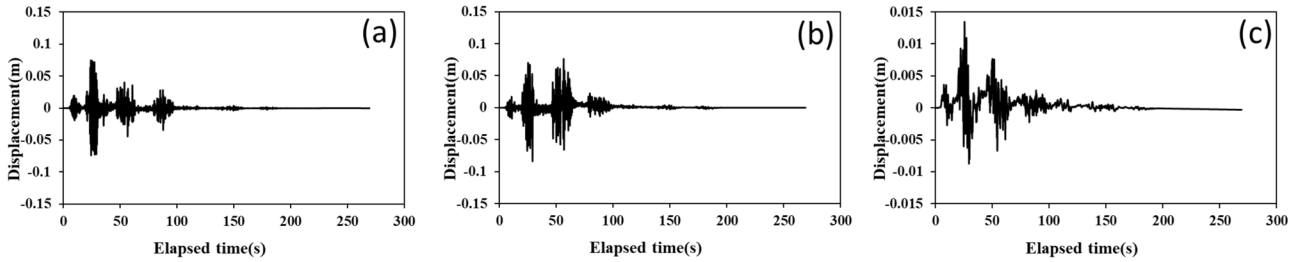

Fig. 22 Response displacements of **a** transversal direction to dam axis, **b** direction of dam axis, and **c** vertical direction (Inhomogeneous model)

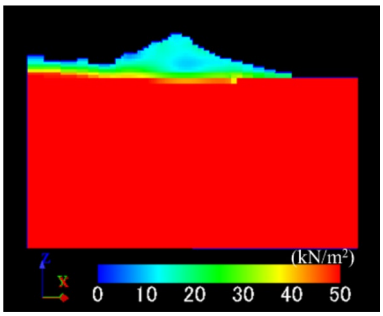

Fig. 23 Distribution of deviatoric stress second invariants of center section (Homogeneous model)

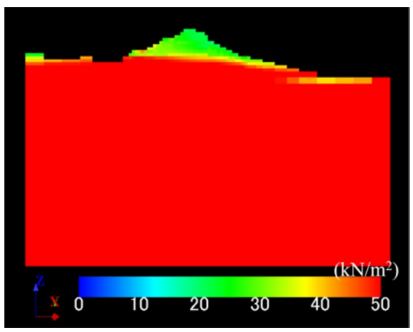

Fig. 24 Distribution of deviatoric stress second invariants of center section (Inhomogeneous model)

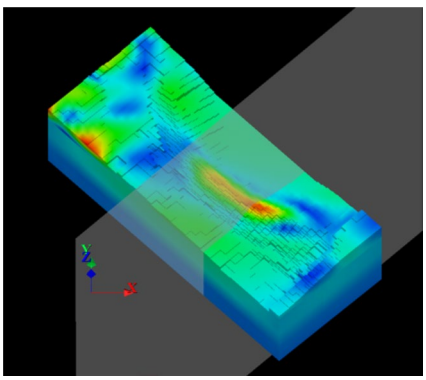

Fig. 25 Cross section of area of acceleration concentration (Inhomogeneous model)

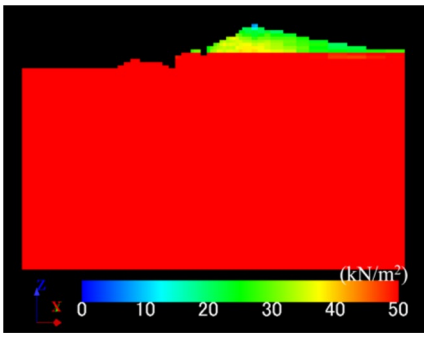

Fig. 26 Distribution of deviatoric stress second invariants in area of acceleration concentration (Inhomogeneous model)

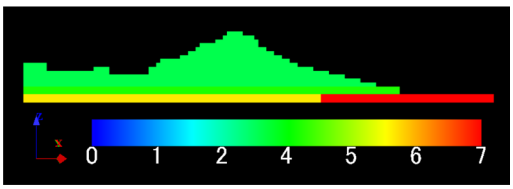

Fig. 27 N-values of center section (Homogeneous model)

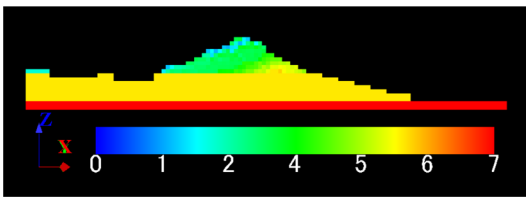

Fig. 28 N-values of center section (Inhomogeneous model)

where J_2 is the second invariant of the deviatoric stress (kN/m^2). Parameters σ_x, σ_y, and σ_z are the effective stresses in the x-axis, y-axis, and z-axis directions (kN/m^2), respectively. Parameters τ_{xy}, τ_{yz}, and τ_{zx} are the shear stresses in the xy-plane, yz-plane, and zx-plane (kN/m^2), respectively. Figures 23 and 24 provide the $\sqrt{2J_2}$ distribution of the central section. Figure 25 shows the cross section of the area where the acceleration concentration occurs, while Fig. 26 shows the $\sqrt{2J_2}$ distribution of the cross section where the acceleration concentration occurs. Finally, Figs. 27 and 28 present the N-value distributions of the central section for the homogeneous and inhomogeneous models, respectively, while Fig. 29 displays the N-value distribution of the

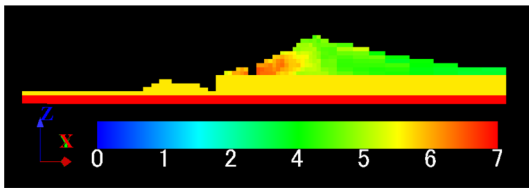

Fig. 29 N-values in area of concentrated acceleration (Inhomogeneous model)

acceleration-concentrated cross section for the inhomogeneous model.

An examination of the acceleration distribution maps (Figs. 15 and 16) reveals that both models exhibit significant acceleration concentration at shallow depths, particularly at the embankment crest. The inhomogeneous model (Fig. 16) demonstrates more pronounced acceleration concentration on the left side for the downstream near the spillway, attributable to the structural division caused by the spillway feature.

The acceleration waveforms for the inhomogeneous model (Fig. 18) indicate that accelerations in both transversal and axial directions exceed 6 m/s^2. Notably, the transversal acceleration surpasses 10 m/s^2, suggesting more pronounced behavior in the transversal direction compared to the embankment axial direction at the central crest node. When compared to the homogeneous model (Fig. 17), the inhomogeneous model exhibits lower accelerations in the axial and vertical directions, but higher acceleration in the transversal direction at the central crest node.

A comparison of the response velocity waveforms (Figs. 19 and 20) indicates minimal differences between the models; however, the inhomogeneous model demonstrates greater transversal velocity at the earthquake peak. Similarly, the response displacement waveforms show a limited variation between the models, although the homogeneous model exhibits greater axial displacement at the earthquake peak (Figs. 21 and 22).

Comparing the $\sqrt{2J_2}$ distributions in the central sections of the inhomogeneous and homogeneous models, it is seen that the larger $\sqrt{2J_2}$ is found in the cross section of the inhomogeneous model (Figs. 23 and 24). The reasons are supposed to be that the base ground is set up considering the SWS test results and that the N-value of the crown section is relatively small in the inhomogeneous model.

In the distribution of $\sqrt{2J_2}$ in the cross section (Fig. 25), where the acceleration is concentrated, a large value for $\sqrt{2J_2}$ appears inside the embankment (Fig. 26). A distribution of relatively high N-values is found in the acceleration-concentrated section (Fig. 29) compared with the N-values in the center section (Figs. 27 and 28).

Collectively, these findings indicate that the inhomogeneous model reveals significant seismic effects on the embankment near the spillway, identifying this region as particularly vulnerable to shear stress. Although a large value for $\sqrt{2J_2}$ is seen at the foundation in the figures, it is caused by the large initial stress, and does not mean instability.

Summary and conclusions

(1) A three-dimensional finite element model was successfully constructed by extending topographic measurement data to subsurface regions using drone-based three-dimensional measurements.
(2) Comprehensive geotechnical investigation results, aligned with the three-dimensional model, were obtained through screw weight sounding (SWS) tests. The spatial distributions of the embankment and the ground stiffness parameters were subsequently estimated using statistical modeling with Gaussian process regression (GPR).
(3) An inhomogeneous model was developed from the SWS test results and subjected to a seismic response analysis. For comparative purposes, a model homogeneous along the embankment axis was also developed based on standard penetration test results.

The comparative analysis demonstrated that the inhomogeneous model exhibited localized acceleration concentration, indicating that spatial heterogeneity significantly influences the seismic response characteristics. The $\sqrt{2J_2}$ distribution maps identified potential weak points within the embankment structure with respect to shear stress resistance. Furthermore, detailed ground modeling precisely localized the region of maximum acceleration concentration on the left side of the bank for the downstream near the spillway.

(4) The spatial distribution of the ground stiffness estimated in the present study is the average representation, and estimated seismic response of the ground is average image due to the average properties. Although the empirical transformation equations to estimate stiffness include the great uncertainty, and the ground stiffness includes the inherent spatial uncertainty, the present study deals with the average properties of the soil parameters. The variability in the estimated stiffness parameters may influence the magnitude and localization of the seismic response, especially crest acceleration and shear stress concentration. Future studies will investigate parameter sensitivity and uncertainty propagation within the proposed framework.

Funding This work was supported by Grant-in-Aid for Scientific Research, Grant Numbers 20H00442 and 24H00534 (Representative: Shin-ichi Nishimura) from the Japan Society for the Promotion of Science (JSPS) KAKENHI.

Open Access This article is licensed under a Creative Commons Attribution 4.0 International License, which permits use, sharing, adaptation, distribution and reproduction in any medium or format, as long as you give appropriate credit to the original author(s) and the source, provide a link to the Creative Commons licence, and indicate if changes were made. The images or other third party material in this article are included in the article's Creative Commons licence, unless indicated otherwise in a credit line to the material. If material is not included in the article's Creative Commons licence and your intended use is not permitted by statutory regulation or exceeds the permitted use, you will need to obtain permission directly from the copyright holder. To view a copy of this licence, visit http://creativecommons.org/licenses/by/4.0/.

References

Chen Q, Wang C, Juang CH (2015) CPT-based evaluation of liquefaction potential accounting for soil spatial variability at multiple scales. J Geotech Geoenviron Eng 142:04015077. https://doi.org/10.1061/(ASCE)GT.1943-5606.0001402

Chen J, Liu P, Xu Q, Li J (2020) Seismic analysis of hardfill dams considering spatial variability of material parameters. Eng Struct. https://doi.org/10.1016/j.engstruct.2020.110439

Ching J, Yoshida I, Phoon KK (2022) Comparison of trend models for geotechnical spatial variability: sparse Bayesian learning vs. Gaussian process regression. Gondwana Res. https://doi.org/10.1016/j.gr.2022.07.011

Development Group of Liquefaction Analysis Code LIQCA (2021) Data of LIQCA3D21 (in Japanese)

Duvenaud D, Lloyd JR, Grosse R, Tenenbaum JB, Ghahramani Z (2013) Structure discovery in nonparametric regression through compositional kernel search. Proceedings of the 30th International Conference on Machine Learning, pp 1166–1174

Guan Z, Wang Y (2022) CPT-based probabilistic liquefaction assessment considering soil spatial variability, interpolation uncertainty and model uncertainty. Comput Geotech 141:104504. https://doi.org/10.1016/j.compgeo.2021.104504

Inada M (1960) Usage of Swedish weight sounding results: soil mechanics and foundation engineering. Journal of JSSMGE 8(1):13–18

JGS 1435 (2012) Japanese Geotechnical Society Standards, geotechnical and geoenvironmental investigation methods

Jiang Q, Rong M, Wei W, Chen T (2024) A quantitative seismic topographic effect prediction method based upon BP neural network algorithm and FEM simulation. J Earth Sci 35(4):1355–1366

JIS A 1221 (2020) Japanese Geotechnical Society Standards, geotechnical and geoenvironmental investigation methods

Kaneshige M, Nishimura S, Shibata T, Shuku T (2021) Finite element modelling of an earth-fill dam based on 3-dimensional measurement and seismic response analysis. Trans Jpn Soc Irrigation Drainage Rural Eng 89(1):I_181-I_189. https://doi.org/10.11408/jsidre.89.I_181. **((in Japanese))**

Mosadegh L, Chakraborty S, Puppala AJ (2021) Effect of geomaterial variability on seismic response analyses of earthen dams. Eng Geol. https://doi.org/10.1016/j.enggeo.2021.106513

Nishimura S, Takayama Y, Suzuki M, Murakami A, Fujisawa K (2009) Evaluation of spatial variability of strength in an embankment by synthesis of surface wave method and sounding. Proceeding of 44th JGS annual meeting, pp 133–134 (in Japanese)

Ohashi R, Nishimura S, Kaneshige M, Shibata T, Shuku T (2022) Seismic response analysis of earth dams with geostatistical method and 3-D survey. J Jpn Soc Civ Eng: Ser C (Geosphere Eng) 78(2):140–152 **((in Japanese))**

Orense RP, Yasin M, Suemasa N (2019) Screw driving sounding: a new test for field characterisation. Geotech Res 6(1):28–38. https://doi.org/10.1680/jgere.18.00024

Rasmussen CE, Williams CKI (2006) Gaussian processes for machine learning. MIT Press, London

Japan Road Association (2012). Specifications for highway bridges, I and IV (in Japanese)

Vanmarcke EH (2010) Random fields: Analysis and synthesis. Revised and expanded, new. World Scientific Publishing, Beijing

Xu B, Zou D, Liu H (2012) Three-dimensional simulation of the construction process of the Zipingpu concrete face rockfill dam based on a generalized plasticity model. Comput Geotech. https://doi.org/10.1016/j.compgeo.2012.03.002

Yoshida I, Tomizawa Y, Otake Y (2021) Estimation of trend and random components of conditional random field using Gaussian process regression. Comput Geotech 136:104179. https://doi.org/10.1016/j.compgeo.2021.104179

Zhao T, Wang Y, Xu L (2021) Efficient CPT locations for characterizing spatial variability of soil properties within a multilayer vertical cross-section using information entropy and Bayesian compressive sensing. Comput Geotech. https://doi.org/10.1016/j.compgeo.2021.104260

Zhao T, Song C, Xu L, Huang X (2026) Bayesian selection of the optimal composite kernels for probabilistic estimation of UCS with explicit consideration of measurement errors and the anisotropic characteristic of input features. Georisk 20(1):361–383

Publisher's Note Springer Nature remains neutral with regard to jurisdictional claims in published maps and institutional affiliations.